Letter

# Crystallization via cavity-assisted infinite-range interactions

Paolo Molignini,[1,2,*] Camille Lévêque,[3,4] Hans Keßler,[5] Dieter Jaksch,[1] R. Chitra,[6] and Axel U. J. Lode[7]

[1]*Clarendon Laboratory, Department of Physics, University of Oxford, Parks Roads, Oxford OX1 3PU, United Kingdom*
[2]*Cavendish Laboratory, Department of Physics, University of Cambridge, JJ Thomson Road, Oxford OX1 3PU, United Kingdom*
[3]*Wolfgang Pauli Institute c/o Faculty of Mathematics, University of Vienna, Oskar-Morgenstern-Platz 1, 1090 Vienna, Austria*
[4]*Vienna Center for Quantum Science and Technology, Atominstitut, TU Wien, Stadionallee 2, 1020 Vienna, Austria*
[5]*Zentrum für Optische Quantentechnologien and Institut für Laser-Physik, Universität Hamburg, 22761 Hamburg, Germany*
[6]*Institute for Theoretical Physics, ETH Zurich, 8093 Zurich, Switzerland*
[7]*Institute of Physics, Albert-Ludwig University of Freiburg, Hermann-Herder-Strasse 3, 79104 Freiburg, Germany*

(Received 9 July 2021; revised 3 February 2022; accepted 31 May 2022; published 13 July 2022)

We study a one-dimensional array of bosons with infinite-range interactions mediated by a laser-driven dissipative optical cavity. The cavity-mediated infinite-range interactions open up an alternative pathway to crystallization, hitherto only known for dipolar bosons due to their long-range interactions. In parameter ranges attainable in state-of-the-art experiments, we systematically compare observables for bosons and fermions with infinite-range interactions. At sufficiently large laser pump powers, many observables, including density distributions in real and momentum space, correlation functions, eigenvalues of the one-body density matrix, and superradiance order parameters, become identical for bosons and fermions. We map out the emergence of this cavity-induced crystallization as a function of pump power and contact interactions. We discover that cavity-mediated interactions can compensate a reduction by several orders of magnitude in the strength of the contact interactions needed to trigger crystallization.

DOI: 10.1103/PhysRevA.106.L011701

Quantum gases coupled to high-finesse optical cavities are increasingly becoming the go-to platform to realize and test nonequilibrium many-body phases of matter [1]. This is due to their ability to dynamically craft strong light-matter interactions with tunable ranges beyond conventional solid-state implementations. After the pioneering realization of the Hepp-Lieb superradiant phase transition of the open Dicke model [2–14], recent developments have highlighted supersolid states with broken continuous symmetries [15–19], quantum crystalline phases [20–23], correlated phases with spinor condensates [24–30], synthetic gauge potentials and topological states [31–48], quasicrystalline order [49–51], and dynamical instabilities [52–59].

Particularly interesting phenomena for quantum gases occur in lower-dimensional geometries, for example for bosons with strongly repulsive contact interactions confined in one dimension (1D). Experimentally, this can be achieved by very tight confinement potentials along the spatial directions to be frozen out [60,61]. Due to the reduced dimensionality, quantum effects become enhanced and the repulsive interactions lead to a so-called Tonks-Girardeau (TG) gas, where bosons acquire certain fermionic characteristics: bosonic density distributions and two-body correlations coincide with those of noninteracting spinless fermions in real space—but not in momentum space. The bosonic contact interactions emulate an effective Pauli exclusion principle, and a Bose-Fermi mapping between the corresponding real-space wave functions can be formulated [62,63]. The existence of the TG gas has been predicted in theoretical studies [64–73] and verified experimentally [74–76]. More recently, it was extended to dynamical systems [77] and even used to generate topological pumping [78].

A related phenomenon was discovered in bosons with dipolar interactions (DIs) [68,69,73,79–88]. In this case, the bosons are first driven into a TG-like state by the short-distance part of the repulsions [68,79,80]. With stronger interactions, the long-range tail of the DIs pushes the particles into a different, strongly correlated Luttinger liquid phase often termed the *crystal state* [69,81–85]. The crystal state has additional attributes to those of the TG state: in contrast to the case with contact interactions, in the crystal state both the real *and* momentum space distributions become equal to those of fermions, and a lack of correlation is seen in both the diagonal *and* off-diagonal elements of correlation functions [73,84,86–88].

In this Letter, we reveal an alternate pathway to crystallization by subjecting bosons to infinite-range cavity-mediated interactions (CMIs). This cavity-assisted crystallization (CAC) occurs *without* a preliminary transition to a TG-like state, and is instead driven by the infinite-range nature of the interactions. Assisted by CMIs, this type of crystallization does not require DIs either, and weak contact interactions are instead sufficient to trigger it. Unlike in the TG-like state, in the CAC state both real- and momentum-space density distributions simultaneously become progressively indistinguishable from their fermionic counterparts. Furthermore, the indistinguishability extends to density fluctuations, one-body and two-body

*pm728@cam.ac.uk

 

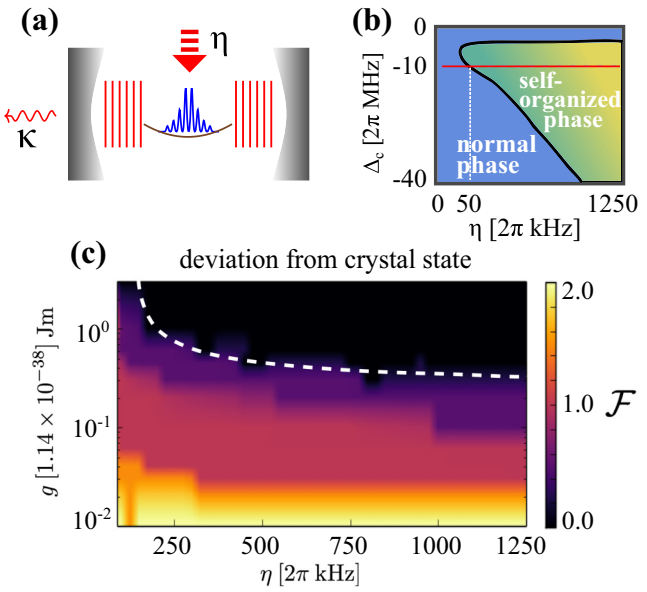


FIG. 1. (a) Schematic setup of parabolically trapped ultracold bosons placed in an optical cavity with loss rate $\kappa$ and driven transversally with a laser pump $\eta$. (b) Sketch of the sweep (red line) in parameter space used for the simulations. The color gradient in the self-organized phase indicates the progression towards CAC. (c) Degree of crystallization $\mathcal{F} \equiv \int |\rho^F(x) - \rho^B(x)| dx$ as a function of $(\eta, g)$. Above the dashed line, $\mathcal{F} = 0$ and CAC is fully achieved, with bosonic and fermionic densities becoming indistinguishable.

correlations, and orbital occupation. Additionally, a complex interplay between different types of interactions emerges: it is possible to lower by up to one order of magnitude the contact interaction strength needed for crystallization if the CMIs are correspondingly increased. The advantages of the cavity system are thus manifold. An easily tunable laser setup can directly trigger crystallization, and we have also the flexibility of operating with a wider range of contact interactions. This is of practical utility, as experimental realizations are often limited by density-dependent three-body losses. Operating with smaller contact interactions allows for lower densities. Our results extend the realm of cold-atom quantum simulators exploiting strong light-matter coupling to crystallization phenomena, and they illustrate the potential of the simulators to engineer even more fascinating states of matter.

We consider a 1D gas of $N$ parabolically trapped ultracold bosons in an optical cavity with a single mode of frequency $\omega_c$ and wave vector $k_c$. The particles are in the dispersive regime and subject to Rayleigh scattering with coherent light of frequency $\omega_p$ pumped transversally to the cavity axis. The particles are confined by an external harmonic potential $V_{\text{trap}}(x) = \frac{1}{2} m\omega_x^2 x^2$, and they interact repulsively through a weak contact interaction of strength $g$. Figure 1(a) illustrates a sketch of the system. The coherent part of the system in the rotating frame can be described by the following Hamiltonian [14,89]:

$$\hat{\mathcal{H}} = \int dx\, \hat{\Psi}^\dagger(x) \left\{ \frac{p^2}{2m} + V_{\text{trap}}(x) + \frac{g}{2} \hat{\Psi}^\dagger(x)\hat{\Psi}(x) \right\} \hat{\Psi}(x)$$
$$+ \hbar \frac{g_0^2}{\Delta_a} \hat{a}^\dagger \hat{a} \int dx\, \hat{\Psi}^\dagger(x)\hat{\Psi}(x)\cos^2(k_c x)$$
$$+ \hbar\eta(\hat{a} + \hat{a}^\dagger) \int dx\, \hat{\Psi}^\dagger(x)\hat{\Psi}(x)\cos(k_c x) - \hbar\Delta_c \hat{a}^\dagger \hat{a}. \quad (1)$$

Here, $\hat{\Psi}(x)^{(\dagger)}$ denotes bosonic field operators at position $x$, and $\hat{a}^{(\dagger)}$ describes the light field of the cavity. The parameter $\eta$ is the two-photon Rabi frequency describing the fluctuations of the light-atom interaction, and it drives crystallization. In the following, we refer to $\eta$ as pump power for simplicity. $\Delta_c$ is the detuning between the pump frequency and the cavity resonance frequency. It is chosen to be negative to operate in the self-organization regime [9,14]. The parameter $g_0$ is the atom-cavity coupling strength for a maximally coupled atom, while $\Delta_a$ is the atom-pump detuning. We choose $\Delta_a$ large enough to justify the rotating-wave approximation and neglect input noise from the cavity (see below). (While we have performed our simulations in the blue-detuned regime $\Delta_a > 0$, we expect our results to be unaffected by the sign of $\Delta_a$ as long as we operate in the regime where $|\Delta_c| \gg |N g_0^2/\Delta_a|$ and the infinite-range interactions dominate.)

The cavity field obeys the equation of motion

$$\frac{\partial}{\partial t}\hat{a} = [i\Delta_c - iU_0\hat{\mathcal{B}} - \kappa]\hat{a} - i\eta\hat{\Theta}, \quad (2)$$

where $\hat{\mathcal{B}} = \int dx\, \hat{\Psi}^\dagger(x)\hat{\Psi}(x)\cos^2(k_c x)$ and $\hat{\Theta} = \int dx\, \hat{\Psi}^\dagger(x)\hat{\Psi}(x)\cos(k_c x)$, $U_0 \equiv \frac{g_0^2}{\Delta_a}$, and we have incorporated the dissipation from the cavity with a phenomenological decay rate $\kappa$ assuming low saturation and negligible input noise [89,90]. To capture the steady-state physics of Eq. (1), we can adiabatically eliminate the cavity field by setting $\partial_t \hat{a} = 0$. To justify this approximation, we work in the limit $\hbar\kappa \gg \hbar^2 k_c^2/2m$ that describes the lossy cavity as adiabatically following the atomic motion [14,89]. The steady-state solution of the cavity field is then [14,89]

$$\hat{a} = \eta[\Delta_c - U_0\hat{\mathcal{B}} + i\kappa]^{-1}\hat{\Theta}. \quad (3)$$

By inserting Eq. (3) back into the Hamiltonian Eq. (1) and considering the limit of large detuning $|\Delta_c| \gg NU_0$, we obtain an effective Hamiltonian where the cavity induces an infinite-range two-body interaction between the particles [14,90,91]:

$$\hat{\mathcal{H}} = \int dx\, \hat{\Psi}^\dagger(x) \left\{ \frac{p^2}{2m} + \frac{g}{2}\hat{\Psi}^\dagger(x)\hat{\Psi}(x) + V_{\text{trap}}(x) \right\} \hat{\Psi}(x)$$
$$+ \frac{\hbar\eta^2(\Delta_c - \mathcal{B}U_0)}{(\Delta_c - \mathcal{B}U_0)^2 + \kappa^2} \int dx\, dx'\, \hat{\Psi}^\dagger(x)\hat{\Psi}^\dagger(x')$$
$$\times \cos(k_c x)\cos(k_c x')\hat{\Psi}(x)\hat{\Psi}(x'). \quad (4)$$

We have approximated the operator $\hat{\mathcal{B}}$ by its expectation value, the bunching parameter $\mathcal{B} = \langle\hat{\mathcal{B}}\rangle$ [14,89]. The ground-state properties of the effective Hamiltonian (4) describe the steady-state solution of the cavity-atom system [90].

We first consider the ground state of the Hamiltonian (4) in the limit where the infinite-range interactions dominate over all other energy scales, $\eta \to \infty$. The integrand of the interaction can be rewritten in terms of relative coordinate $x_{\text{rel}} \equiv$

$x - x'$ and center-of-mass coordinate $x_{\rm cm} \equiv (x + x')/2$ to be $V\cos(k_c x)\cos(k_c x') = \frac{V}{2}[\cos(k_c x_{\rm rel}) + \cos(2k_c x_{\rm cm})]$ [90]. Deep in the red-detuned cavity region $-\Delta_c > N|U_0|$, we have $V < 0$. The relative-coordinate part of the interaction is thus minimized when the particles arrange themselves into a 1D lattice with spacing $2\pi/k_c$. This configuration is then further pinned by the center-of-mass-coordinate part [9,14,90,92]. In the limit of very large CMIs, each particle is thus confined to spatially ordered, nonoverlapping single-particle states. We thus expect the physical attributes of bosons and fermions to coalesce.

We now move away from the fully localized regime to understand the pathway to crystallization when CMIs compete with the kinetic, potential, and short-range interaction parts of the Hamiltonian. To that end, we investigate the ground state of the Hamiltonian (4) with the multiconfigurational time-dependent Hartree method for indistinguishable particles software (MCTDH-X) [93–98] to obtain the steady-state properties as a function of *finite* pump power $\eta$. MCTDH-X works with an adaptive basis set of $M$ time-dependent single-particle states termed "orbitals." With a single orbital $M = 1$, MCTDH-X is equivalent to a mean-field Gross-Pitaevskii description, while as $M \to \infty$ the method becomes numerically exact [99]. In the CAC state, to describe every localized bosonic particle uncorrelated with the others, we only require $M = N$ orbitals [93–95,100]. To account for possible residual correlation effects, we have utilized $M = N + 4$ orbitals in our simulations. However, we have verified that the population of these additional four orbitals is negligible.

For every value of $\eta$, we perform imaginary-time evolution on the Hamiltonian (4) to obtain the ground state. For every state, we calculate density distributions in position and momentum space,

$$\rho(x) = \rho^{(1)}(x, x)/N \tag{5a}$$

$$\tilde{\rho}(k) = \langle \hat{\Psi}(k)^\dagger \hat{\Psi}(k)\rangle/N, \tag{5b}$$

as well as Glauber one-body correlation functions

$$g^{(1)}(x, x') = \frac{\rho^{(1)}(x, x')}{\sqrt{\rho^{(1)}(x, x)\rho^{(1)}(x', x')}}, \tag{6}$$

where $\rho^{(1)}(x, x')$ is the one-body reduced density matrix in position space, which is defined as $\rho^{(1)}(x, x') = \langle \hat{\Psi}^\dagger(x)\hat{\Psi}(x')\rangle$. Similar results for Glauber two-body correlation functions are presented in the supplemental material [99]. We present here results from MCTDH-X simulations of $N = 8$ particles with $M = 12$ orbitals, although we remark that the qualitative properties of the CAC state are not affected by the number of particles.

To better understand the emergence of crystallization, we systematically compare our results for bosons to the ground-state properties of the fermionic counterpart of Hamiltonian (4). We vary the pump power $\eta$ in the interval $2\pi \times [25, 1250]$ kHz, as shown in Figs. 1(b) and 1(c). All remaining parameters are listed in Table I. While our results are valid for any kind of bosonic species, we chose the system parameters in line with possible state-of-the-art experiments with $^{87}$Rb atoms. [Note that most experiments operate with a negative light shift $U_0$, while our simulations were carried out for a positive light shift (blue-detuned regime). However, we expect our results to be unaffected by the sign of $U_0$ as long as we operate in the red-detuned regime where $|\Delta_c| \gg |NU_0|$ and the infinite-range interactions dominate.]

TABLE I. Parameters used in the MCTDH-X simulations.

| Parameter | Value |
|---|---|
| mass $m$ | $6.46 \times 10^{-27}$ kg |
| trapping frequency $\omega_x$ | $2\pi \times 252$ Hz |
| cavity detuning $\Delta_c$ | $-2\pi \times 10.1$ MHz |
| atomic light shift $U_0 \equiv \frac{g_0^2}{\Delta_a}$ | $2\pi \times 2.52$ kHz |
| cavity decay rate $\kappa$ | $2\pi \times 1.30$ MHz |
| contact interaction strength $g$ | $1.14 \times [10^{-38}, 10^{-41}]$ J m |
| pump power $\eta$ | $2\pi \times [25, 1250]$ kHz |

Figure 2 shows the density distribution in real and momentum space of the Bose and Fermi system as a function of the pump power $\eta$. In real space, Figs. 2(a)–2(c), both gases first rapidly self-organize into one of the two possible $\mathbb{Z}_2$-symmetry-breaking configurations that minimize the energy cost due to the CMIs [9,14]. This transition occurs approximately around the same value $\eta \approx 50\,[2\pi$ kHz]. In the self-organized state, the population of the lattice sites at intermediate values of $\eta$ is strongly dependent on the quantum statistics; compare Figs. 2(a), 2(b), and 2(c). Fermions tend to first form pairs of states at the bottom of the trap, but then quickly occupy the outer sites of the lattice, completely localizing into structures with single particles per site. The density distribution for bosons [Fig. 2(b)], instead, expands more slowly and undergoes more rounds of sublattice switching. The bosons completely localize into single-particle states only at much higher values of the pump power $\eta \approx 150\,[2\pi$ kHz]. At this point, the bosonic density distribution becomes indistinguishable from the fermionic one [Fig. 2(c)]. These density profiles agree with single-shot simulations of the full-density

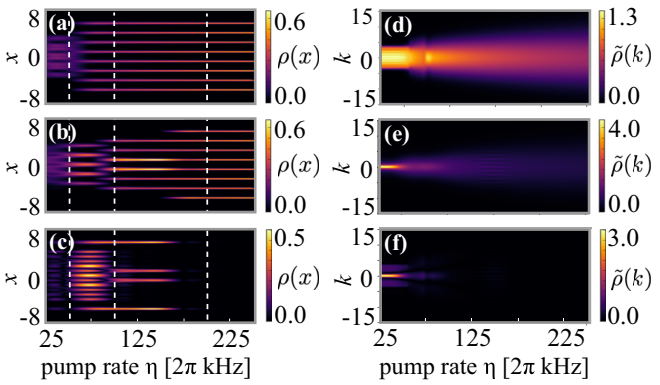


FIG. 2. Comparison of $N = 8$ infinite-range interacting bosons and fermions in terms of real-space density (left panels) and momentum-space density (right panels) as a function of $\eta$: (a) real-space fermionic density, (b) real-space bosonic density, (c) real-space density difference between bosons and fermions, (d) momentum-space fermionic density, (e) momentum-space bosonic density, (f) momentum-space density difference between bosons and fermions. The vertical white dashed lines indicate values of $\eta$ for which correlation functions are plotted in Fig. 3.

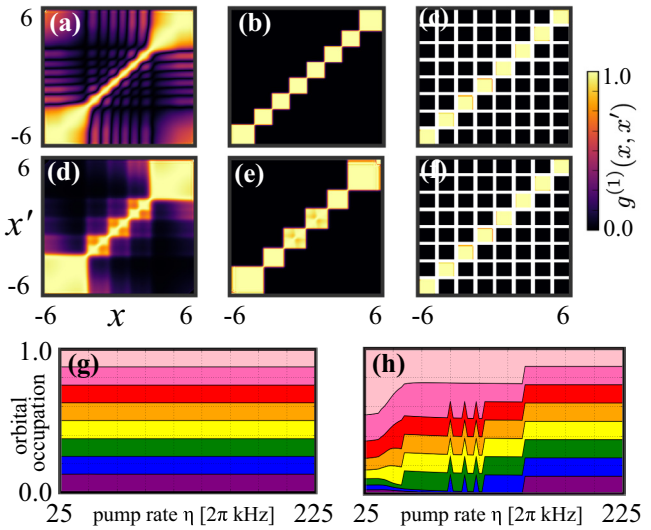


FIG. 3. (a)–(f) Glauber one-body correlation functions in real space at the pump powers indicated in Fig. 2 for $N = 8$ fermions [(a)–(c)] and bosons [(d)–(f)]. The white spaces are introduced to filter numerical singularities where the denominator is $<10^{-7}$. (g),(h) Orbital occupation as a function of pump power for fermions (left) and bosons (right).

distributions, revealing in particular the effective Pauli exclusion principle that bosons obey at high pump powers [99].

Further proof of the equivalence between fermionic and bosonic gases in the ultrastrong CMI limit is offered by the momentum space density, illustrated in Figs. 2(d)–2(f). From this figure, we can clearly see that the momentum distributions for the two types of particles are different at low pump powers, but they rapidly converge to the same Gaussian profile at higher values of $\eta$. From around $\eta \approx 75\,[2\pi$ kHz], the momentum density distributions coincide, unlike in the TG state [65,74].

We now turn to the comparison of the one-body correlations, presented in Fig. 3. Up to intermediate pump powers, $g^{(1)}$ behaves differently for bosons and fermions. However, in the limit of very strongly interacting particles, both systems are described by uncorrelated single-particle states, as ascertained from the completely diagonal form of $g^{(1)}$. As CAC emerges, bosons and fermions also reach the same orbital occupations [panels (g) and (h)], defined as the eigenvalues of the one-body density matrix, $\rho^{(1)}(x, x')$ [96,99]. This result is consistent with the behavior of spinless fermions occupying the lattice minima, and with the Pauli principle that nullifies the many-body effects of long-range interactions. The picture that comes out consistently from all calculated quantities is that the bosons at very high pump-rate $\eta \gtrsim 150\,[2\pi$ kHz] behave exactly like fermions in terms of density distribution and correlations. Note that CAC can be pushed to values of the pump power as low as $\eta \approx 25\,[2\pi$ kHz] by decreasing the number of particles (e.g., to $N = 4$), dissipation, and cavity detuning.

We remark that the CAC state differs from the dipolar crystal state in many ways. Whereas DIs are long- but finite-range, CMIs are truly infinite-range. The infinite-range nature triggers changes in *both* real-space and momentum-space distribution *simultaneously*. In contrast, in dipolar crystallization, it is first the short-range part of the repulsion that triggers a TG-like state, affecting only the real-space density distribution. Only once the long-range part of the DIs starts to dominate are the bosons further pushed into the full crystal state. The energetics is also different. In CAC, the interaction energy increases quadratically, while the kinetic energy increases only linearly with the interaction strength [99]. In dipolar crystallization, the increase in the interaction energy is (super)exponential, while the kinetic energy increases approximately logarithmically [88]. Cavities also offer different ways to control and manipulate interactions over a large region and thus offer more flexibility compared to DIs.

We now comment on the emergence of crystallization as a function of *both* pump power and contact interactions. This is depicted in the effective phase diagram of Fig. 1(c), by means of an effective degree of crystallization,

$$\mathcal{F} \equiv \int dx\, |\rho^F(x) - \rho^B(x)|, \tag{7}$$

that quantifies the difference between the fermionic real-space density $\rho^F(x)$ and its bosonic counterpart $\rho^B(x)$. The black region in the figure (delineated by the dashed white line) indicates complete crystallization with $\mathcal{F} \approx 0$ and indistinguishable densities among the different quantum particles. By mapping the continuum system to an effective Bose-Hubbard lattice model, we have verified that crystallization occurs when the on-site repulsion dominates over hopping and local chemical potential [99].

As compared to standard TG physics, CMIs facilitate the appearance of crystallization at lower values of contact interaction $g$. As illustrated in Fig. 1(c), for a pump power of $\eta \approx 1250 \times 2\pi$ kHz, the contact interaction $g$ needed to enter the crystal state is reduced by one order of magnitude in comparison to a smaller pump strength of $\eta \approx 200 \times 2\pi$ kHz. This phase diagram, besides offering a roadmap for the experimental realization of the CAC state, provides numerical evidence of how infinite-range interactions can drastically decrease the strength of the contact interactions needed to achieve such a state.

In summary, we have illustrated an alternative pathway to crystallization for ultracold bosons via cavity-mediated infinite-range interactions driven by an external laser. As the pump power of the driving laser is gradually increased, the bosons become progressively indistinguishable from fermions in terms of density distributions in both real and momentum space, orbital occupations, and Glauber correlation functions. We have mapped out the crystal state as a function of pump power and contact interactions, revealing an intriguing interplay whereby crystallization can be achieved with one order of magnitude smaller contact interactions by correspondingly increasing the pump power.

For our simulations, we explicitly considered parameter ranges consistent with the setups realized in the experiments of Ref. [9]. Although a larger dissipation facilitates the emergence of crystallization, we expect other experiments with lower dissipation, such as the ones performed in Ref. [92], to lead to qualitatively similar results. The use of a wider parabolic trap is another expedient that would facilitate the observation of the CAC state. Single-shot images should

offer a practical way to probe crystallization experimentally [101]. Relevant observables such as one- and two-body densities could be either accessed directly via averaging over single-shot images, or reconstructed with the help of machine learning [102]. Furthermore, single-shot images give access to full-distribution functions [86,87], where the emergent Pauli principle would manifest naturally. Our study exemplifies the power and flexibility of cavity-mediated interactions to achieve ultrastrong interacting regimes in ultracold quantum-light matter systems, and it should pave the way for further experimental investigation of crystallization phenomena.

As CAC is obtained without optical lattices, they can instead be employed to investigate other effects, such as lattice incommensuration needed to realize Bose glass phases [103,104]. A multimode cavity setup would shift the interaction range from infinite towards long-range [105] and would allow us to probe the effect of tuning the interaction range [106]. We also anticipate that the cavity setup could be a robust arena to investigate crystallization dynamically [77].

We acknowledge financial support from the Swiss National Science Foundation (SNCF), Giulio Anderheggen, the Austrian Science Foundation (FWF) under Grant No. F65 (SFB "Complexity in PDEs"), Grant No. F41 (SFB "ViCo"), Grant No. DFG-KE2481/1-1, and Grant No. P32033-N32, and the Wiener Wissenschafts- und TechnologieFonds (WWTF) Project No. MA16-066 ("SEQUEX"). P.M. acknowledges funding from the ESPRC Grant No. EP/P009565/1. We also acknowledge the computation time on the ETH Euler and HLRS Stuttgart clusters. This work was partially funded by the European Research Council under the European Union's Seventh Framework Programme/ERC Grant Agreement No. 319286 Q-MAC.

[1] F. Mivehvar, F. Piazza, T. Donner, and H. Ritsch, Adv. Phys. **70**, 1 (2021).
[2] R. H. Dicke, Phys. Rev. **93**, 99 (1954).
[3] K. Hepp and E. H. Lieb, Ann. Phys. **76**, 360 (1973).
[4] Y. K. Wang and F. T. Hioe, Phys. Rev. A **7**, 831 (1973).
[5] H. Carmichael, C. Gardiner, and D. Walls, Phys. Lett. A **46**, 47 (1973).
[6] S. Ritter, F. Brennecke, K. Baumann, T. Donner, C. Guerlin, and T. Esslinger, Appl. Phys. B **95**, 213 (2009).
[7] T. P. Purdy, D. W. C. Brooks, T. Botter, N. Brahms, Z.-Y. Ma, and D. M. Stamper-Kurn, Phys. Rev. Lett. **105**, 133602 (2010).
[8] D. Nagy, G. Kónya, G. Szirmai, and P. Domokos, Phys. Rev. Lett. **104**, 130401 (2010).
[9] K. Baumann, C. Guerlin, F. Brennecke, and T. Esslinger, Nature (London) **464**, 1301 (2010).
[10] J. Keeling, M. J. Bhaseen, and B. D. Simons, Phys. Rev. Lett. **112**, 143002 (2014).
[11] J. Klinder, H. Keßler, M. Wolke, L. Mathey, and A. Hemmerich, Proc. Natl. Acad. Sci. (USA) **112**, 3290 (2015).
[12] A. U. J. Lode and C. Bruder, Phys. Rev. Lett. **118**, 013603 (2017).
[13] P. Molignini, L. Papariello, A. U. J. Lode, and R. Chitra, Phys. Rev. A **98**, 053620 (2018).
[14] R. Lin, L. Papariello, P. Molignini, R. Chitra, and A. U. J. Lode, Phys. Rev. A **100**, 013611 (2019).
[15] J. Léonard, A. Morales, P. Zupancic, T. Esslinger, and T. Donner, Nature (London) **543**, 87 (2017).
[16] E. I. Rodriguez Chiacchio and A. Nunnenkamp, Phys. Rev. A **98**, 023617 (2018).
[17] F. Mivehvar, S. Ostermann, F. Piazza, and H. Ritsch, Phys. Rev. Lett. **120**, 123601 (2018).
[18] A. Morales, P. Zupancic, J. Léonard, T. Esslinger, and T. Donner, Nat. Mater. **17**, 686 (2018).
[19] S. C. Schuster, P. Wolf, S. Ostermann, S. Slama, and C. Zimmermann, Phys. Rev. Lett. **124**, 143602 (2020).
[20] A. Kollár, A. Papageorge, V. Vaidya, Y. Guo, J. Keeling, and B. Lev, Nat. Commun. **8**, 14386 (2017).
[21] V. D. Vaidya, Y. Guo, R. M. Kroeze, K. E Ballantine, A. J Kollar, J. Keeling, and B. L. Lev, Phys. Rev. X **8**, 011002 (2018).
[22] Y. Guo, R. M. Kroeze, V. D. Vaidya, J. Keeling, and B. L. Lev, Phys. Rev. Lett. **122**, 193601 (2019).
[23] P. Karpov and F. Piazza, Phys. Rev. A **100**, 061401(R) (2019).
[24] F. Mivehvar, F. Piazza, and H. Ritsch, Phys. Rev. Lett. **119**, 063602 (2017).
[25] M. Landini, N. Dogra, K. Kroeger, L. Hruby, T. Donner, and T. Esslinger, Phys. Rev. Lett. **120**, 223602 (2018).
[26] A. U. J. Lode, F. S. Diorico, R. Wu, P. Molignini, L. Papariello, R. Lin, C. Lévêque, L. Exl, M. C. Tsatsos, R. Chitra *et al.*, New J. Phys. **20**, 055006 (2018).
[27] R. M. Kroeze, Y. Guo, V. D. Vaidya, J. Keeling, and B. L. Lev, Phys. Rev. Lett. **121**, 163601 (2018).
[28] E. Colella, R. Citro, M. Barsanti, D. Rossini, and M. L. Chiofalo, Phys. Rev. B **97**, 134502 (2018).
[29] E. Colella, S. Ostermann, W. Niedenzu, F. Mivehvar, and H. Ritsch, New J. Phys. **21**, 043019 (2019).
[30] N. Masalaeva, W. Niedenzu, F. Mivehvar, and H. Ritsch, Phys. Rev. Research **3**, 013173 (2021).
[31] Y. Deng, J. Cheng, H. Jing, and S. Yi, Phys. Rev. Lett. **112**, 143007 (2014).
[32] L. Dong, L. Zhou, B. Wu, B. Ramachandhran, and H. Pu, Phys. Rev. A **89**, 011602(R) (2014).
[33] F. Mivehvar and D. L. Feder, Phys. Rev. A **89**, 013803 (2014).
[34] F. Mivehvar and D. L. Feder, Phys. Rev. A **92**, 023611 (2015).
[35] C. Kollath, A. Sheikhan, S. Wolff, and F. Brennecke, Phys. Rev. Lett. **116**, 060401 (2016).
[36] A. Sheikhan, F. Brennecke, and C. Kollath, Phys. Rev. A **93**, 043609 (2016).
[37] A. Sheikhan, F. Brennecke, and C. Kollath, Phys. Rev. A **94**, 061603(R) (2016).
[38] W. Zheng and N. R. Cooper, Phys. Rev. Lett. **117**, 175302 (2016).
[39] K. E. Ballantine, B. L. Lev, and J. Keeling, Phys. Rev. Lett. **118**, 045302 (2017).
[40] C. M. Halati, A. Sheikhan, and C. Kollath, Phys. Rev. A **96**, 063621 (2017).
[41] F. Mivehvar, H. Ritsch, and F. Piazza, Phys. Rev. Lett. **118**, 073602 (2017).
[42] L. W. Clark, B. M. Anderson, L. Feng, A. Gaj, K. Levin, and C. Chin, Phys. Rev. Lett. **121**, 030402 (2018).

[43] F. Görg, K. Sandholzer, J. Minguzzi, R. Desbuquois, M. Messer, and T. Esslinger, Nat. Phys. **15**, 1161 (2019).

[44] F. Mivehvar, H. Ritsch, and F. Piazza, Phys. Rev. Lett. **122**, 113603 (2019).

[45] C. M. Halati, A. Sheikhan, and C. Kollath, Phys. Rev. A **99**, 033604 (2019).

[46] E. Colella, F. Mivehvar, F. Piazza, and H. Ritsch, Phys. Rev. B **100**, 224306 (2019).

[47] F. Schlawin and D. Jaksch, Phys. Rev. Lett. **123**, 133601 (2019).

[48] K. Wintersperger, C. Braun, F. N. Ünal, A. Eckardt, M. D. Liberto, N. Goldman, I. Bloch, and M. Aidelsburger, Nat. Phys. **16**, 1058 (2020).

[49] F. Mivehvar, H. Ritsch, and F. Piazza, Phys. Rev. Lett. **123**, 210604 (2019).

[50] K. Viebahn, M. Sbroscia, E. Carter, J.-C. Yu, and U. Schneider, Phys. Rev. Lett. **122**, 110404 (2019).

[51] M. Sbroscia, K. Viebahn, E. Carter, J.-C. Yu, A. Gaunt, and U. Schneider, Phys. Rev. Lett. **125**, 200604 (2020).

[52] F. Piazza and H. Ritsch, Phys. Rev. Lett. **115**, 163601 (2015).

[53] E. I. R. Chiacchio and A. Nunnenkamp, Phys. Rev. Lett. **122**, 193605 (2019).

[54] H. Keßler, J. G. Cosme, M. Hemmerling, L. Mathey, and A. Hemmerich, Phys. Rev. A **99**, 053605 (2019).

[55] P. Zupancic, D. Dreon, X Li, A. Baumgärtner, A. Morales, W. Zheng, N. R. Cooper, T. Esslinger, and T. Donner, Phys. Rev. Lett. **123**, 233601 (2019).

[56] B. Buča and D. Jaksch, Phys. Rev. Lett. **123**, 260401 (2019).

[57] R. Lin, P. Molignini, A. U. J. Lode, and R. Chitra, Phys. Rev. A **101**, 061602(R) (2020).

[58] K. Wintersperger, M. Bukov, J. Näger, S. Lellouch, E. Demler, U. Schneider, I. Bloch, N. Goldman, and M. Aidelsburger, Phys. Rev. X **10**, 011030 (2020).

[59] H. Keßler, P. Kongkhambut, C. Georges, L. Mathey, J. G. Cosme, and A. Hemmerich, Observation of a Dissipative Time Crystal, Phys. Rev. Lett. **127**, 043602 (2021).

[60] A. Görlitz, J. M. Vogels, A. E. Leanhardt, C. Raman, T. L. Gustavson, J. R. Abo-Shaeer, A. P. Chikkatur, S. Gupta, S. Inouye, T. Rosenband, and W. Ketterle, Phys. Rev. Lett. **87**, 130402 (2001).

[61] M. Greiner, I. Bloch, O. Mandel, T. W. Hänsch, and T. Esslinger, Phys. Rev. Lett. **87**, 160405 (2001).

[62] M. D. Girardeau and M. Olshanii, arXiv:cond-mat/0309396.

[63] V. I. Yukalov and M. D. Girardeau, Laser Phys. Lett. **2**, 375 (2005).

[64] M. Girardeau, J. Math. Phys. **1**, 516 (1960).

[65] A. Lenard, J. Math. Phys. **5**, 930 (1964).

[66] L. Pollet, S. M. A. Rombouts, and P. J. H. Denteneer, Phys. Rev. Lett. **93**, 210401 (2004).

[67] O. E. Alon and L. S. Cederbaum, Phys. Rev. Lett. **95**, 140402 (2005).

[68] S. Zöllner, H.-D. Meyer, and P. Schmelcher, Phys. Rev. A **74**, 053612 (2006).

[69] F. Deuretzbacher, K. Bongs, K. Sengstock, and D. Pfannkuche, Phys. Rev. A **75**, 013614 (2007).

[70] S. Zöllner, H.-D. Meyer, and P. Schmelcher, Phys. Rev. A **78**, 013629 (2008).

[71] G. Zürn, F. Serwane, T. Lompe, A. N. Wenz, M. G. Ries, J. E. Bohn, and S. Jochim, Phys. Rev. Lett. **108**, 075303 (2012).

[72] R. Roy, A. Gammal, M. C. Tsatsos, B. Chatterjee, B. Chakrabarti, and A. U. J. Lode, Phys. Rev. A **97**, 043625 (2018).

[73] S. Bera, B. Chakrabarti, A. Gammal, M. C. Tsatsos, M. Lekala, B. Chatterjee, C. Lévêque, and A. U. J. Lode, Sci. Rep. **9**, 17873 (2019).

[74] B. Paredes, A. Widera, V. Murg, O. Mandel, S. Fölling, I. Cirac, G. V. Shlyapnikov, T. W. Hänsch, and I. Bloch, Nature (London) **429**, 277 (2004).

[75] T. Kinoshita, T. Wenger, and D. S. Weiss, Science **305**, 1125 (2004).

[76] T. Jacqmin, J. Armijo, T. Berrada, K. V. Kheruntsyan, and I. Bouchoule, Phys. Rev. Lett. **106**, 230405 (2011).

[77] J. M. Wilson, N. Malvania, Y. Le, Y. Zhang, M. Rigol, and D. S. Weiss, Science **367**, 1461 (2020).

[78] W. Kao, K.-Y. Li, K.-Y. Lin, S. Gopalakrishnan, and B. L. Lev, Science **371**, 296 (2021).

[79] A. S. Arkhipov, G. E. Astrakharchik, A. V. Belikov, and Y. E. Lozovik, J. Exp. Theor. Phys. Lett. **82**, 39 (2005).

[80] Y. Hao, Y. Zhang, J. Q. Liang, and S. Chen, Phys. Rev. A **73**, 063617 (2006).

[81] R. Citro, E. Orignac, S. DePalo, and M. L. Chiofalo, Phys. Rev. A **75**, 051602(R) (2007).

[82] P. Pedri, S. DePalo, E. Orignac, R. Citro, and M. L. Chiofalo, Phys. Rev. A **77**, 015601 (2008).

[83] J. Schachenmayer, I. Lesanovsky, A. Micheli, and A. J. Daley, New J. Phys. **12**, 103044 (2010).

[84] F. Deuretzbacher, J. C. Cremon, and S. M. Reimann, Phys. Rev. A **81**, 063616 (2010).

[85] G. E. Astrakharchik and Y. E. Lozovik, Phys. Rev. A **77**, 013404 (2008).

[86] B. Chatterjee and A. U. J. Lode, Phys. Rev. A **98**, 053624 (2018).

[87] B. Chatterjee, M. C. Tsatsos, and A. U. J. Lode, New J. Phys. **21**, 033030 (2019).

[88] B. Chatterjee, J. Schmiedmayer, C. Lévêque, and A. U. J. Lode, Phys. Rev. Lett. **125**, 093602 (2020).

[89] C. Maschler, I. B. Mekhov, and H. Ritsch, Eur. Phys. J. D **46**, 545 (2008).

[90] R. Mottl, Ph.D. thesis, ETH Zürich 2014.

[91] I. B. Mekhov, C. Maschler, and H. Ritsch, Nat. Phys. **3**, 319 (2007).

[92] J. Klinder, H. Keßler, M. R. Bakhtiari, M. Thorwart, and A. Hemmerich, Phys. Rev. Lett. **115**, 230403 (2015).

[93] O. E. Alon, A. I. Streltsov, and L. S. Cederbaum, Phys. Rev. A **77**, 033613 (2008).

[94] A. U. J. Lode, Phys. Rev. A **93**, 063601 (2016).

[95] E. Fasshauer and A. U. J. Lode, Phys. Rev. A **93**, 033635 (2016).

[96] R. Lin, P. Molignini, L. Papariello, M. C. Tsatsos, C. Lévêque, S. E. Weiner, E. Fasshauer, R. Chitra, and A. U. J. Lode, Quantum Sci. Technol. **5**, 024004 (2020).

[97] A. U. J. Lode, C. Lévêque, L. B. Madsen, A. I. Streltsov, and O. E. Alon, Rev. Mod. Phys. **92**, 011001 (2020).

[98] A. U. J. Lode, M. C. Tsatsos, E. Fasshauer, S. E. Weiner, R. Lin, L. Papariello, P. Molignini, C. Lévêque, M. Büttner, J. Xiang, and S. Dutta, MCTDH-X: The MultiConfigurational Time-Dependent Hartree Method for Indistinguishable Particles Software (2022).

[99] See Supplemental Material at http://link.aps.org/supplemental/10.1103/PhysRevA.106.L011701 for results for Glauber two-body correlation functions.
[100] A. U. J. Lode, K. Sakmann, O. E. Alon, L. S. Cederbaum, and A. I. Streltsov, Phys. Rev. A **86**, 063606 (2012).
[101] K. Sakmann and M. Kasevich, Nat. Phys. **12**, 451 (2016).
[102] A. U. J. Lode, R. Lin, M. Büttner, L. Papariello, C. Lévêque, R. Chitra, M. C. Tsatsos, D. Jaksch, and P. Molignini, Optimized observable readout from single-shot images of ultracold atoms via machine learning, Phys. Rev. A **104**, L041301 (2021).
[103] H. Habibian, A. Winter, S. Paganelli, H. Rieger, and G. Morigi, Phys. Rev. A **88**, 043618 (2013).
[104] H. Habibian, A. Winter, S. Paganelli, H. Rieger, and G. Morigi, Phys. Rev. Lett. **110**, 075304 (2013).
[105] P. Karpov and F. Piazza, arXiv:2106.13226.
[106] U. R. Fischer, A. U. J. Lode, and B. Chatterjee, Phys. Rev. A **91**, 063621 (2015).